Wall shear stress measurements and parametric analysis of impinging wall jets

J.B.R. Loureiro [a,b,*], A.P. Silva Freire [a]

[a] Mechanical Engineering Program (PEM/COPPE/UFRJ), C.P. 68503, 21941-972 Rio de Janeiro, Brazil
[b] Mechanical Engineering Department (DEM/Poli/UFRJ), C.P. 68503, 21941-972 Rio de Janeiro, Brazil

ARTICLE INFO

ABSTRACT

This paper investigates the influence of some governing parameters on the near wall characteristics of a circular impinging jet onto a smooth flat plate. Laser Doppler anemometry (LDA) is used to characterize the mean and turbulent fields including the wall shear stress. The experiments were conducted at one nozzle-to-plate space ($H/D = 2$) and Reynolds number of 47,100. The work makes a parametric analysis of impinging jets based on (i) conventional parameters that include the nozzle diameter, the nozzle-to-plate distance and the bulk velocity of the jet and (ii) gross parameters like the jet momentum flux. Parametrization schemes based on conventional quantities are shown to be very sensitive to the particular choice of reference quantity, resulting in functional behaviours that can be represented through either power law or linear expressions. On the other hand, it is shown that the jet momentum flux and the kinematic viscosity suffice to determine the mean and fluctuating flow parameters, even in the initial region of wall jet development ($1 < r/D < 5$). With the latter choice, the streamwise variation of the maximum mean velocity and maximum Reynolds longitudinal stress are shown to decay according to power law expressions. A particular near wall parametrization scheme for the mean velocity profile that resorts to a scaling procedure based on the stream-wise evolution of the flow characterized by its maximum velocity is also presented. Higher-order moments of the velocity fluctuations are discussed.

© 2012 Elsevier Ltd. All rights reserved.

1. Introduction

Turbulent jets impinging onto flat, smooth surfaces have been studied in connection with many industrial applications. Their inherent capacity of enhancing heat and mass transfer has stimulated research into many relevant aspects of the problem. For instance, the effects of Reynolds number and of the aspect ratio H/D on the local Nusselt number distribution are topics of considerable interest. For this reason, they have attracted much attention, having been discussed for many flow configurations.

However, and despite the consistently high number of works that have been published in the past, some basic issues still remain to be adequately addressed. One of these, and a very important one, concerns the distribution of the wall shear stress. The scarcity of reference data for the wall shear stress distribution beneath an impinging jet has been particularly emphasized by Guo and Wood [1]. In addition to their own data, Guo and Wood cite the works of Tu and Wood [2] and Phares et al. [3].

Measurement of the wall shear stress can present surprising difficulties for non-equilibrium turbulent boundary layers. The very fine near wall scale that defines the characteristics of attached turbulent flows, of the order of v/u_τ (u_τ = friction velocity), frequently causes many problems associated with practicality and accuracy. Previous studies by Winter [4], Naughton and Sheplak [5] and Hutchins and Choi [6] have reviewed in detail available techniques based on direct measurement, momentum balance, wall similarity and liquid tracers. The development, advantages and limitations of the techniques are discussed under the perspective of present and future uses.

It is of interest to note that for non-equilibrium flows the only reliable way to determine the local wall shear stress is to measure the velocity profile in the viscous sublayer. This method is even not violated by strong adverse pressure gradients and separated flows. The very small measurement volume of modern laser Doppler anemometers means that results with great spatial and temporal resolution can be obtained. For example, Loureiro et al. [7] and Loureiro et al. [8] have measured the wall shear stress distribution for separated flow around a steep hill.

Six wall shear stress measurement techniques are reviewed by Loureiro et al. [9] for flow over a changing surface, from rough to smooth. Again, the usefulness of the viscous sublayer approach is emphasized. Loureiro et al. [9] show that, through laser Doppler anemometry (LDA), ten points can be used to characterize the flow to within 500 μm of the wall.

The purpose of this paper is twofold. First, some very detailed near wall laser Doppler anemometry measurements are conducted to evaluate the wall shear stress – τ_w – by means of the linear mean

* Corresponding author at: Mechanical Engineering Program (PEM/COPPE/UFRJ), C.P. 68503, 21941-972 Rio de Janeiro, Brazil. Tel.: +55 21 3622 3548.
E-mail addresses: jbrloureiro@gmail.com, jbrloureiro@mecanica.coppe.ufrj.br (J.B.R. Loureiro).

Nomenclature

A, A_1, A_2	parameters in velocity law of the wall
b	half-width of the impingement pressure profile
B_1, B_2	parameters in power law expression
C_1, C_2	parameters in power law expression
d	Preston tube diameter
D	nozzle diameter
D_1, D_2	parameters in power law expression
F	flatness
H	nozzle-to-plate distance
n_1, n_2	parameters in power law expression
m_1, m_2	parameters in power law expression
M_j	jet momentum flux ($=DU_o^2$)
P	impingement pressure
r	radial distance
R_D	Reynolds number ($=U_oD/v$)
s	parameter in Weibull distribution
S	skewness
U, u	longitudinal velocity component
u_τ	friction velocity
x, y	flow cartesian coordinates

Greek symbols

β	parameter in Weibull distribution
η	parameter in Weibull distribution
$\varkappa$	von Karman's constant ($=0.4$)
v	kinematic viscosity
ρ	density
τ	shear stress
ζ	$=r/b$.

Subscripts

0.5	position of the half-velocity
max	local maximum
o	jet bulk condition
rms	root-mean square
u	longitudinal velocity
w	wall condition

Superscripts

'	fluctuating quantity

velocity profile in the viscous sublayer. Second, a parametric analysis of impinging jets is made based on procedures that take into account conventional parameters such as the nozzle diameter, the nozzle-to-plate distance and the bulk velocity of the jet, or that, alternatively, consider some gross parameters like the jet momentum flux. A study of the near wall logarithmic solution in terms of the parameters proposed by Özdemir and Whitelaw [10] is also made.

The first objective aims at obtaining reference data that can be used in the future to validate near wall analytical and numerical models. Wall shear stress, mean velocity and higher-order statistics are presented. The second objective improves the work of Guerra et al. [11], where a self-dependent procedure was used to evaluate τ_w. In Guerra et al. [11], the velocity and temperature fields of a confined impinging jet were studied. For the first time, an analogy between the near wall behaviour of the velocity and temperature profiles was established. Logarithmic profiles were then proposed for both fields based on conventional parameters, e.g., the friction velocity and friction temperature. A fundamental difficulty in Guerra et al. [11] was the determination of the friction velocity, which was evaluated from the slope of the proposed near wall velocity solution. Here, an independent assessment of u_τ is made through the linear portion of the velocity profile. Only after that, the functional behaviour of the logarithmic solution is studied.

The different parametrization schemes that are studied in the present work are applied to the mean and fluctuating quantities of the flow. The turbulent field, in particular, is shown to be very sensitive to the choice of reference quantities, provided the conventional parameters are considered. An analysis based on gross parameters, however, shows that the jet momentum flux and the kinematic viscosity suffice to determine the mean and fluctuating flow parameters, even in the initial region of wall jet development ($1 < r/D < 5$). In the later case, the streamwise variation of the maximum mean velocity and maximum Reynolds longitudinal stress are shown to decay according to power law expressions.

The Preston tube has been used by Tu and Wood [2] and Guo and Wood [1] to evaluate the wall shear stress. Here, Preston tube measurements of τ_w are compared to the LDA-estimates to assess the usefulness of the former technique.

2. Velocity field wall function

One particularly serious difficulty in turbulence modelling, which is in fact common to all wall bounded flows, rests on the description of the fine flow length-scales in the near wall region. The use of wall functions implies that just one length-scale equation needs to be specified. The great appeal of this scheme is the large computational economy that results. Also, and as an extra bonus, wall functions provide a relatively simple and reliable way to determine the wall shear stress.

In the past years, many substitutions for the wall function approach have been suggested in literature. For example, Chen and Jaw [12] describe ten alternative procedures based on low-Reynolds number models. These models try to account for wall-vicinity and viscous effects with the introduction of damping functions, which, unfortunately, require the use of very fine grids, introduce additional non-linearity and do not have a universal character (Popovac and Hanjalic [13], Craft et al. [14]). The resulting numerical stiffness and increase in computational time frequently render this approach of no use for industrial applications. Against this background, many new treatments of the wall boundary conditions have been proposed to include non-equilibrium effects. Typical instances are the recent contributions of Chedevergne [15], Popovac and Hanjalic [13] and Craft et al. [14].

For the specific case of wall jets, Patel [16], Tailland and Mathieu [17], Ozarapoglu [18] and Irwin [19] reported the existence of a velocity logarithmic region. However, none of these authors mutually agreed on the appropriate functional behaviour for the log-law intercept, A. The failure of the conventional logarithmic law for wall jets was also verified by Hammond [20]. A further study on the role of the scaling laws in wall jet flows was carried out by Wygnanski et al. [21].

For an oblique jet, experiments by Özdemir and Whitelaw [10] have shown that a near wall logarithmic region can be observed well clear of the wall up to the point of maximum velocity. Özdemir and Whitelaw also proposed a functional behaviour for the log-law intercept, A, that uses a scaling procedure based on the stream-wise evolution of the flow characterized by its maximum velocity, U_{max}. The important contribution of this work was the recognition that the nozzle diameter is an inappropriate reference

scaling. Thus, local similarity must take into account the flow evolution. To describe the deviation function, Özdemir and Whitelaw [10] proposed an expression of the form:

$$\frac{u}{u_\tau} = \frac{1}{\varkappa} \ln\left(\frac{y u_\tau}{\nu}\right) + A, \qquad (1)$$

with

$$A = A_1 \frac{U_{max}}{u_\tau} - A_2, \qquad (2)$$

where $\varkappa = 0.4$, u_τ denotes the friction velocity and A_1 and A_2 are constants.

The velocity logarithmic behaviour of an orthogonally impinging jet was further investigated experimentally by Guerra et al. [11], who also showed the temperature profile to follow a logarithmic behaviour. From an assessment of more than sixty velocity profiles, the authors found that to achieve near wall similarity the reference velocity scale had to be indeed U_{max}. According to their experiments, $A_1(=1.124)$ and $A_2(=-10.524)$.

3. Flow features and measurement techniques

The experimental apparatus used in this work is basically the same described in Guerra et al. [11] (Fig. 1). A centrifugal blower is used to drive air at 20.0 °C through a 1350 mm long pipe of 43.5 mm internal diameter. A honeycomb and a series of screens are placed immediately downstream of a contraction to set the flow uniform and to control its level of turbulence. For the present experiments, the jet issued from the circular nozzle with a bulk velocity, $U_o = 17 \text{ ms}^{-1}$. These conditions give a Reynolds number based on jet nozzle diameter, R_D, equal to 47,100. (For a two-dimensional nozzle, D is the jet exit gap.)

The impingement smooth flat surface was made of a plexiglass plate with 840 mm in diameter. Only one nozzle-to-plate spacing was considered in the experiments, $H/D = 2$.

3.1. Laser Doppler anemometry

The one-channel laser-Doppler anemometer used a 400 mW Ar-ion tube laser and was operated in the forward-scatter mode. A Bragg cell unit was used to introduce a 40 MHz frequency shift, which was then digitally adjusted to allow correct measurements of near-zero mean velocities. The light beams that emerged from the 60 mm diameter FiberFlow probe passed through a beam translator and a beam expander with expansion ratio of 1.98. These optical components were used to increase the beam spacing and, as a consequence, to provide a smaller measurement volume with higher laser power, maximizing the signal to noise ratio.

Front lens with 800 mm focus length were mounted on the probe to accurately position the measurement volume on the impinging jet centerline. Before reception by the photomultiplier, the scattered light passed through an interference filter of 514.5 nm, so that only the green light was received by the photomultiplier. Table 1 lists the main characteristics of the laser-Doppler system. The signal from the photomultiplier was digitized and processed through a burst spectrum analyzer BSA P60 operating in single measurement per burst mode. The Dantec BSA Flow Software 4.50 was used to calculate the Doppler frequency and the resulting velocity samples. A series of LDA biases were avoided by the use of transit time weighting and by adjusting the strictest parameters on the data processor and software. The level validation and the signal to noise ratio were 8 and 5 respectively. For the statistics at each point, 50,000 samples were acquired.

3.2. Seeding

In the present work, seeding was provided by a Laskin nozzle. This particle generator was filled with an aqueous solution of dialcohol and glycerol. Droplets produced by a Laskin nozzle vary in size, normally between 0.5 to 5.0 μm in diameter. In fact, particle diameter depends on the pressure of the compressed air feeding line and on properties of the working fluid. In the present work,
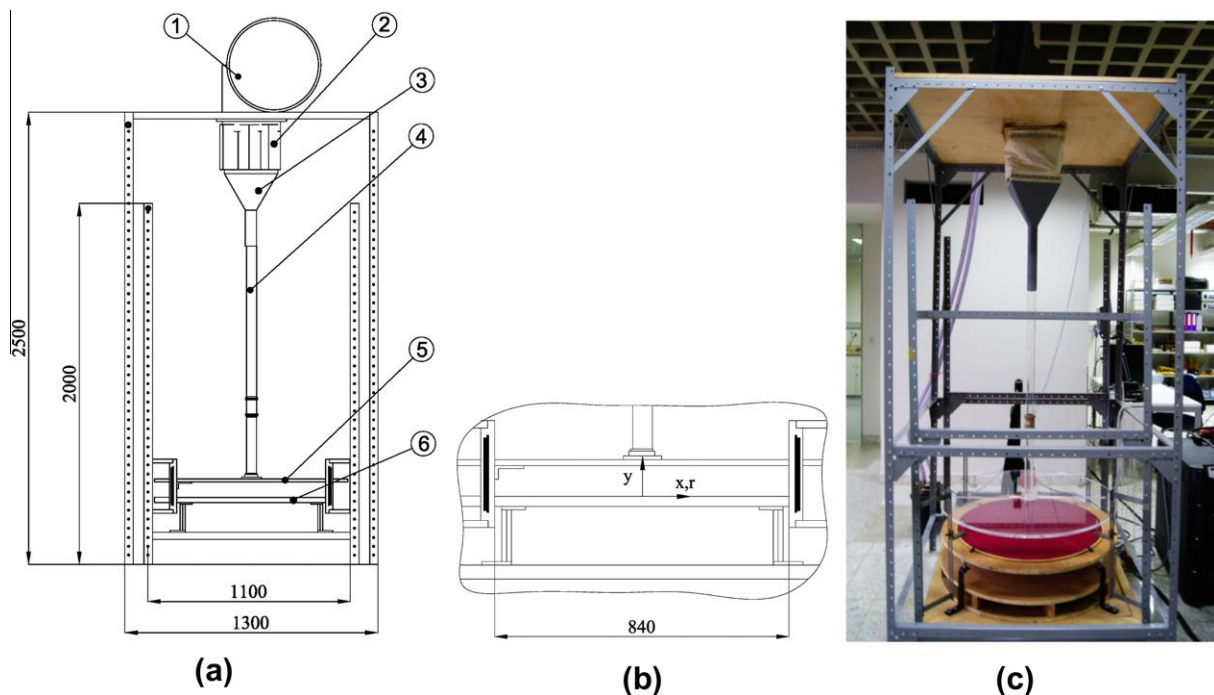

Fig. 1. General arrangement of the experimental set up: (a) descriptive drawing including (1) centrifugal blower, (2) flexible transition section, (3) contraction, (4) flow pipe, (5) confinement plate, (6) impingement plate; (b) schematic detail showing the coordinate system; (c) photograph. Dimensions are shown in mm.

Table 1
Main characteristics of the laser-Doppler system.

Wavelength	514.5 nm
Half-angle between beams	2.69°
Fringe spacing	5.5 μm
Beam spacing	38 mm
Dimensions of the measur. volume	
Major axis	2.56 mm
Minor axis	120.4 μm

a 5 bar pressure input furnished particles of approximately 3 μm in size.

The use of a Laskin nozzle assured a continuously seeded flow with particles that were able to follow the flow field fluctuations but yet scatter enough light to provide a good signal to noise ratio. An investigation for the most appropriate injection position showed that connecting the tracer particles directly to the inlet of the fan furnished the best results.

3.3. Preston sensor

A Preston tube is basically a Pitot tube that is set to rest on a surface to determine the velocity at a known distance from the wall. Then, considering that this velocity measurement is determined uniquely by the surface shear stress, calibration curves can be used to find the friction velocity [4]. The present work used surface Pitot tubes with external diameters of 0.38, 1.26, 1.65 and 3.18 mm. For data reduction, the calibration curves of Patel [22] were used.

Pressure measurements were obtained through a Furness micromanometer, that provided an accuracy of 0.001 Pa.

4. Results and discussion

The wall pressure distribution is shown in Fig. 2 for the jet exit Reynolds number, $R_D = 47,100$. As reported by other authors, the pressure profile follows a Gaussian distribution. Tu and Wood [2] and Guo and Wood [1] have used the half-width of the impingement profile, b, to correlated their wall shear stress data. Since we will be referring often to those works, we have decided to do the same introducing $\zeta = r/b$.

As mentioned before, few works published in literature for impinging jets present data for the skin-friction coefficient. Notable contributions are the papers of Özdemir and Whitelaw [10], Tu and Wood [2], Phares et al. [3] and Guo and Wood [1]. Özdemir and Whitelaw [10] assessed the wall shear stress from observed streaks of pigmented oil which was sprayed uniformly over the experimental surface and exposed to the jet flow. Tu and Wood
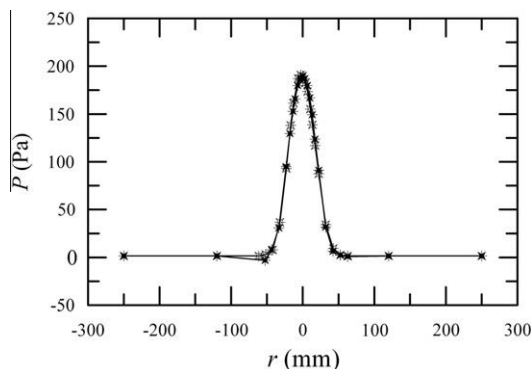
[2] and Guo and Wood [1] used Preston tubes and Stanton probes. For gas jets, Phares et al. [3] observed the removal of monosized spheres.

Here, τ_w is evaluated from the slope of the linear velocity distribution in the viscous region. The uncertainty related to the determination of the absolute distance from the wall due to the finite size of the measurement volume was estimated according to the procedure described in Durst et al. [23]. The consequence is a method that can be used to obtain τ_w with high confidence.

Velocity profiles at eight measuring positions are shown in Fig. 3, in physical and inner flow coordinates respectively. To every profile, at least five measurement points have been located in the first 250 μm of the wall. The resulting friction velocity distribution is shown in Fig. 4 together with results given by the Preston tube readings.

Keeping in mind that at $r = 0$, $u_\tau = 0$, the LDA-measurements indicate that u_τ increases from the origin to $r \approx 75$ mm. For r higher than 75 mm, u_τ decreases up to point $r = 175$ mm, where a slight increase is observed. Our Preston tube measurements, on the other hand, always show a monotonic decrease in u_τ as r increases. The fail to predict the decreasing behaviour of u_τ as r approaches the origin implies that at position $r = 50$ mm, the Preston tube ($d = 1.26$ mm) and LDA results differ by 27%.

The Preston tubes and Stanton probes used by Tu and Wood [2] ranged from 0.46 to 0.92 mm in diameter and 0.05 to 0.13 mm in height, respectively. These authors show that the effect of probe dimension on wall shear stress measurements are significant. In fact, the peak in wall shear stress obtained with the Preston tubes is typically about 40% lower than that measured with a Stanton probe. However, all their data on τ_w exhibit the expected behaviour, irrespective of the dimension of their probes. For $R_D = 6300$, the wall shear stress increases from the origin up to a global maximum located at about, $\zeta_{max} = r_{max}/b = 1.3$, where ζ_{max} is the value of ζ that gives the maximum stress. A local minimum is observed at $\zeta = 3$, followed by a second local maximum at $\zeta = 4.5$. For $R_D = 11,000$, the local minimum practically merges with the second maximum, yielding a curve with an almost monotonically decreasing behaviour.

In the present measurements, the local peak in τ_w, $2\tau_{w_{max}}/(\rho U_o^2) = 0.0066$, is located at $\zeta_{max} = 3.25$. This is followed, as r increases, by a region of nearly constant τ_w, $6.4 < r/b < 8.7$, after which τ_w decreases. For the two-dimensional jet of Tu and Wood [2], this behaviour was observed for $H/D = 5$ and $R_D = 4400$. To our flow conditions, $\tau_{w_{max}}$ is about 1.6 times higher than the values measured by Tu and Wood [2] and Guo and Wood [1].

The work of Tummers et al. [24], only recently came to our attention; their flow parameters for a round unconfined jet are $H/D = 2$ and $R_D = 23,000$. The LDA-measured wall shear stress distribution shows the double peak configuration, with a global maximum $T = 2\tau_{w_{max}}/(\rho U_o^2) = 0.016$ at $\zeta_{max} = 0.5$.

The work of Phares et al. [3] follows the recommendation of some previous authors and suggests the flow domain for an impinging jet to be divided into four regions: the free-jet region, the inviscid impingement region, the impinging boundary layer and the wall-jet region. For the wall jet region, they use the empirical expression of Poreh et al. [25] for the mean shear stress in a radial wall jet,

$$\frac{\tau_w}{\rho U_o^2} = 0.34 R_D^{-3/10} \left(\frac{D}{H}\right)^2 \left(\frac{r}{H}\right)^{-2.3}. \tag{3}$$

Results yielded by Eq. (3) are shown in Fig. 5. The four distinct regions described in Phares et al. [3] were identified with PIV visualization (not shown here). In the jet deflection region, the strong streamline curvatures accelerate the boundary layer until the radial
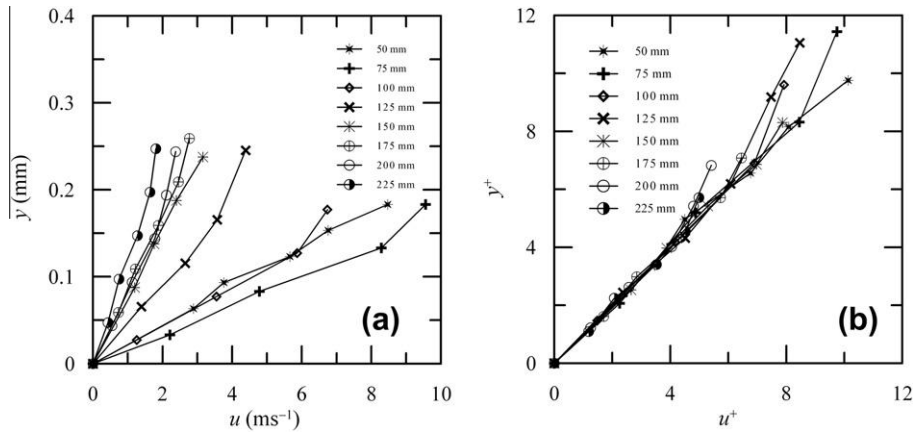

Fig. 2. Impingement pressure distribution.

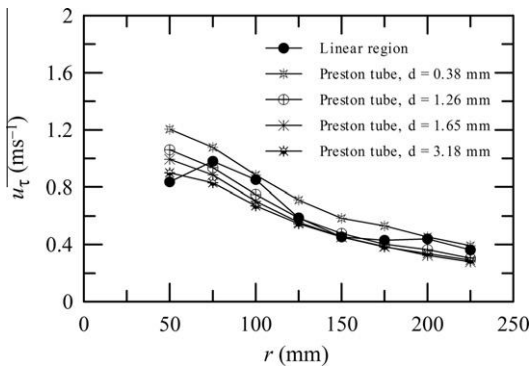**Fig. 3.** Velocity profiles in physical (a) and inner flow coordinates (b).

Fig. 4. Skin-friction velocity over the smooth impingement surface.

spreading starts to decelerate the flow giving rise to the wall-jet structure that was observed to begin development at about $r = 75$ mm. Fig. 5 shows that for $4.0 < r/b < 10$ the empirical prediction of Eq. (3) shows a very good agreement with the experimental results. For $r/b < 4.0$, Eq. (3) predicts values that are within the order of magnitude of the experimental data but that disagree by as much as 50%.

An analysis of the impingement boundary layer based on laminar flow considerations (Phares et al. [3]) gives the magnitude and location of the shear stress maximum, according to

$$\tau_{w_{max}} = 44.6\rho U_o^2 R_D^{-1/2}\left(\frac{H}{D}\right)^{-2}, \quad \frac{r_{max}}{H} = 0.09. \tag{4}$$
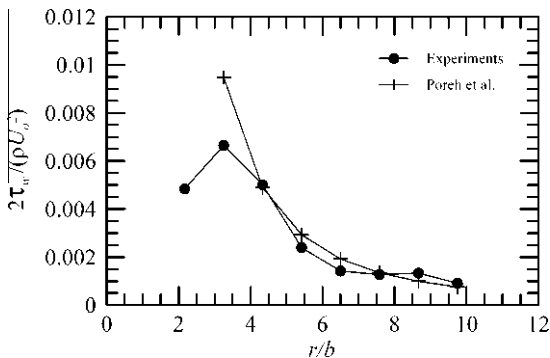
Fig. 5. Wall shear stress distribution: present experimental data and predictions through the empirical expression of Poreh et al. [25].

These expressions have a very limited use since the laminar to turbulent transition that takes place in the impingement region provokes a large increase in wall shear stress. Further arguments for turbulent flow are cited by Phares et al. [3], after Beltaos and Rajaratnam [26], to propose

$$\tau_{w_{max}} = 0.16\rho U_o^2 \left(\frac{D}{H}\right)^2. \tag{5}$$

Eq. (4) furnishes predictions of $T\left(= 2\tau_{w_{max}}/\left(\rho U_o^2\right)\right)$ and ζ_{max} of 0.10 and 0.34 respectively. Eq. (5), on the other hand, gives $T = 0.08$. These estimates are one order of magnitude different from the experimental values of $T = 0.0066$ and $\zeta_{max} = 3.25$ respectively.

The mean velocity distribution for all considered positions are shown in Fig. 6 in physical coordinates. The work of Özdemir and Whitelaw [10] has suggested that a Weibull distribution (Eq. (6)) might represent well some of the global features of the mean velocity profile, such as the position of the maximum and of the outer inflection point ($y_{0.5}$), but is not a suitable approximation in the near wall region, implying an infinite wall shear stress. For this region, we mentioned before, they showed that a semi-logarithmic relation have to be used to model the inner equilibrium layer, Eqs. (1) and (2), in terms of a scaling procedure based on the stream-wise evolution of the flow velocities U_{max} and u_{τ}.
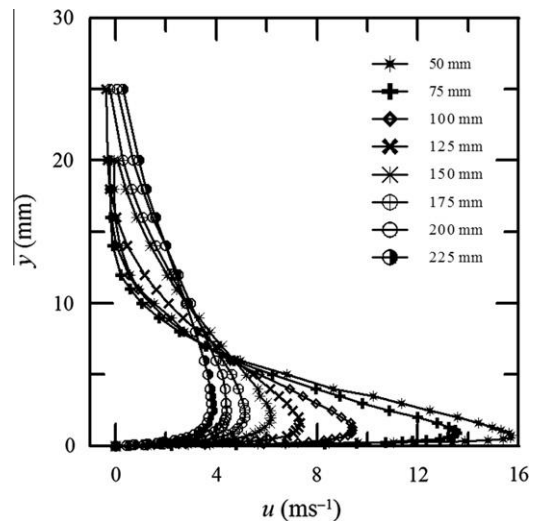

Fig. 6. LDA results for the radial mean velocity profiles at stations $r = 50, 75, 100, 125, 150, 175, 200$ and 225 mm.

Here, we tried to fit the expression proposed by Özdemir and Whitelaw [10] (Eq. (6)) to our data. Unfortunately, we had no success in doing that since a very poor agreement resulted. However, the Weibull distribution can be also described by the simpler form given by Eq. (7). The similarity fit obtained with Eq. (7) is shown in Fig. 7 with $\eta = 1.32$ and $\beta = 0.73$. Incidentally, these values compare well with $\eta = 1.32$ and $s\sqrt{2} = 0.76$ obtained by Özdemir and Whitelaw [10]. Indeed, the features of the outer velocity profile are well described by Eq. (7). The shear stress profile, however, tends to infinity with the $(\eta - 2)$-power as y approaches the wall.

$$\frac{u}{U_{max}} = \frac{(y/y_{0.5})^{\eta-1}}{\left(\frac{\eta-1}{\eta}\right)^{\eta-1/\eta}(s\sqrt{2})^{\eta-1}} \exp\left(-\left(\frac{y/y_{0.5}}{s\sqrt{2}}\right)^{\eta} + \frac{\eta-1}{\eta}\right), \quad (6)$$

$$\frac{u}{U_{max}} = \frac{\eta}{\beta}\left(\frac{y/y_{0.5}}{\beta}\right)^{\eta-1} \exp\left(-\left(\frac{y/y_{0.5}}{\beta}\right)^{\eta}\right). \quad (7)$$

Clearly, the representation of the inner flow requires the development of correlations capable of describing the behaviour of U_{max} and its position, y_{max}, as a function of the radial distance. For the present confined jet conditions, this is made in Fig. 8.

For unconfined turbulent wall jets, many authors have proposed to correlate the results through power law expressions with the forms,

$$\frac{U_{max}}{U_o} = B_1\left(\frac{r}{D}\right)^{n_1}, \quad (8)$$

$$\frac{y_{max}}{D} = B_2\left(\frac{r}{D}\right)^{n_2}. \quad (9)$$

Values quoted for parameters B_1, B_2, n_1 and n_2 vary greatly according to flow conditions. The data in Fig. 8 give $B_1 = 1.203$, $n_1 = -0.989$, $B_2 = 0.010$ and $n_2 = 0.437(1 < r/D < 4)$. Özdemir and Whitelaw [10] found for their unconfined flow conditions, $B_1 = 0.870$, $n_1 = -1.459$, $B_2 = 0.110$ and $n_2 = 1.156$. In fact, in Özdemir and Whitelaw [10], Eq. (9) was used to correlate $y_{0.5}$, the distance from the wall to the point $u = U_{max}/2$.

The choice of U_{max} and D as the basic flow scales has been challenged by Narasimha et al. [27] with the argument of selective memory. These authors reason that sufficiently downstream in turbulent flows "the details of the initial conditions are not relevant, but rather only a few gross parameters which are in some sense dynamically equivalent". The natural implication is that Eqs. (8) and (9) are re-written as
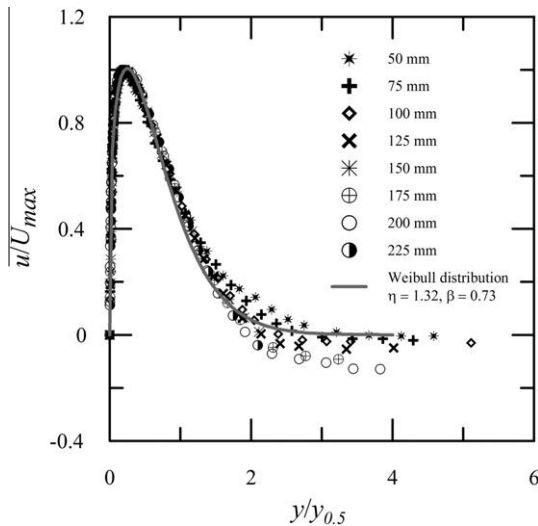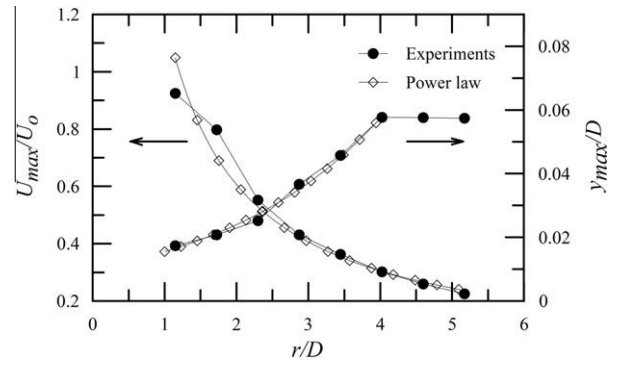

Fig. 8. Functional behaviour of U_{max} and its position, y_{max}, as a function of the radial distance.

$$\frac{U_{max}v}{M_j} = C_1\left(\frac{rM_j}{v^2}\right)^{m_1}, \quad M_j = DU_o^2, \quad (10)$$

$$\frac{y_{max}M_j}{v^2} = C_2\left(\frac{rM_j}{v^2}\right)^{m_2}. \quad (11)$$

Strictly speaking, Eqs. (10) and (11) should only be used for very large values of r/D. Fig. 9, however, shows that even for very small values of the radial distance, the power law fits perfectly well to the experimental data. The suggested values of the flow parameters are: $C_1 = 44974.65$, $m_1 = -0.989$, $C_2 = 0.064$ and $m_2 = 0.928$. For the turbulent unconfined wall jet, Narasimha et al. [27] report $C_1 = 4.6$, $m_1 = -0.506$, $C_2 = 0.096$ and $m_2 = 0.91$.

The exponents for Eqs. (8) and (10) were found to be exactly the same, -0.989, and this is a good indication that U_{max} presents a nearly inversely linear decay with r, in any of the considered propositions. This conclusion does not agree with Özdemir and Whitelaw [10] and Narasimha et al. [27], who found respectively, -1.459 (unconfined impinging jet) and -0.506 (unconfined wall jet). The increase of y_{max} with r in both propositions, Eqs. (9) and (11), is proportional to the exponents 0.437 and 0.928 respectively. For n_2, Özdemir and Whitelaw [10] estimated the value of 1.156, which does not agree with our present findings. However, the values of C_2 and m_2 published by Narasimha et al. agree almost exactly with our present measurements. This indicates that the growth of y_{max} is nearly linear with r in the gross parameter formulation of Narasimha et al. [27].

The relevant flow parameters at all measurement positions are summarized in Table 2.

The present reference data for u_τ can now be used to find the parametric behaviour of A in Eq. (1).
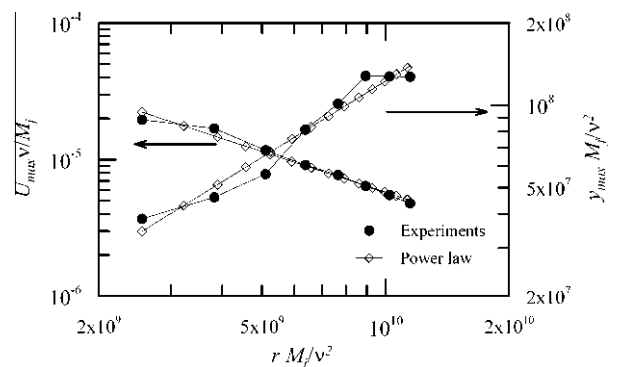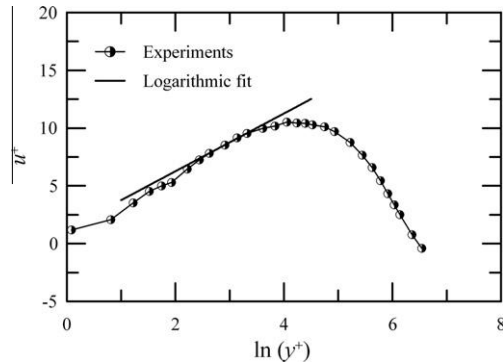

Fig. 7. Weibull distribution for the radial mean velocity profiles.

Fig. 9. Functional behaviour of U_{max} and its position, y_{max}, in the variables proposed by Narasimha et al. [27].

Table 2
Local properties of the flow.

r (mm)	u_τ (ms^{-1})	U_{max} (ms^{-1})	y_{max} (mm)
50	0.8357	15.71	0.753
75	0.9801	13.55	0.903
100	0.8507	9.38	1.097
125	0.5871	7.32	1.595
150	0.4534	6.17	1.98
175	0.4292	5.13	2.509
200	0.4396	4.40	2.504
225	0.3627	3.82	2.497

Fig. 10. Typical curve fit to the mean velocity data: $u^+ = u/u_\tau$, $y^+ = yu_\tau/v$.

Fig. 11. Deviation function for the velocity profiles.

Table 3
Constants A_1 and A_2 in Eq. (2).

Author	A_1	A_2
Özdemir and Whitelaw [10]	1.292	−6.2
Guerra et al. [11]	1.124	−10.524
Present	0.962	−8.987

Fig. 12. Normalized velocity profiles in inner coordinates.

To estimate A, the same procedure described in Loureiro et al. [28] was adopted here. Global optimization algorithms based on direct search methods were used. Despite their tendency to converge more slowly, direct search methods can be more tolerant to the presence of noise in the function and to constraints. Four methods were used to search the solution: nelder mead, differential evolution, simulated annealing and random search. Only when all four methods furnished consistent results, with accuracy down to the sixth decimal place, the search was stopped.
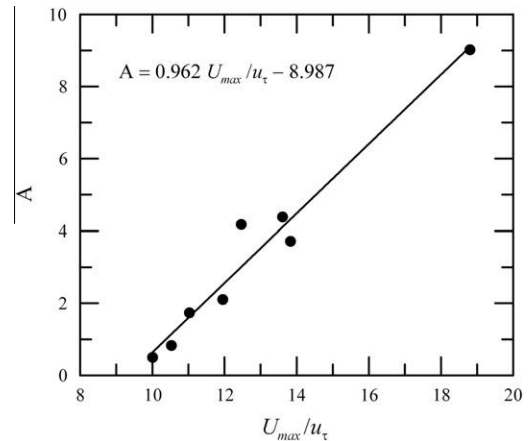
A typical logarithmic fit to the experimental mean velocity profile is shown in a semi-logarithmic plot, Fig. 10. The level of the fitted straight line furnishes the values of A, which can then be used to find A_1 and A_2.

The linear behaviour of A observed in Fig. 11 is used to determine A_1(=0.962) and A_2(=−8.987). These values are compared with the results of Özdemir and Whitelaw [10] and Guerra et al. [11] in Table 3. As a whole, the values in Table 3 are very consistent: A_1 has a value most probably near unity and A_2 around 9. The large variation in values that, for example, Narasimha et al. [27] describe for the coefficients and exponents in correlations such as Eqs. (8) and (9) is not observed for the values shown in Table 3. The relevant conclusion is that the functional behaviour of the additive parameter in the law of the wall for impinging jets over smooth surfaces seems to follow Eq. (12),

$$A = 0.962 \frac{U_{max}}{u_\tau} - 8.987. \qquad (12)$$

When the first term on the right-hand side of Eq. (12) is subtracted from the velocity profiles, the resulting curves collapse in a certain region (Fig. 12), where they show the behaviour of an equilibrium layer.
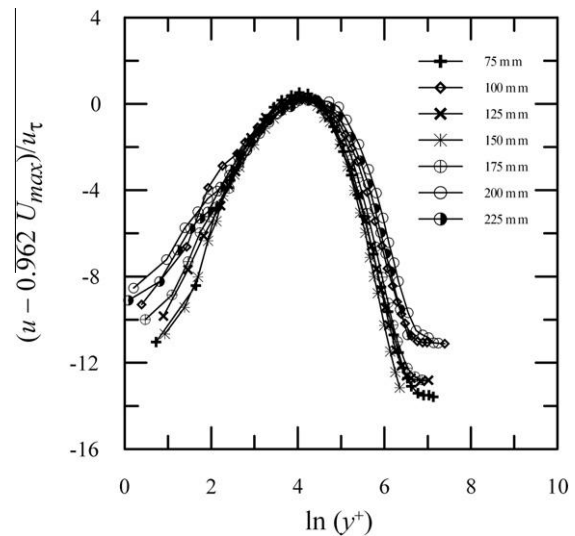
In an impinging jet, the turbulent mixing layer formed between the potential core and the quiescent fluid is well characterized by the turbulent kinetic energy and Reynolds stresses. Close to the stagnation point the favorable pressure gradients suppress turbulence near to the surface. Thus, the main properties of the flow close to the stagnation point are insensitive to the level of turbulence in the free-jet (Kataoka et al. [29]). In fact, the high turbulence levels exhibited in the unsteady shear layer that surrounds the free jet are transfered to the boundary layer, inducing turbulence levels that are much higher than those appearing in a equilibrium boundary layer. This is clearly visible in Fig. 13, where two local maxima can be observed for u'_{rms}, in particular, for $y = 75$, 100 and 125 mm. The existence of a twin peak distribution for u'_{rms} is a well established fact, having been noted by many authors, including Özdemir and Whitelaw [10] and Tummers et al. [24]. At downstream stations the peak in the inner layer weakens, becoming an inflexion point ($r \geqslant 150$ mm). The longitudinal Reynolds stress profiles are then dominated by the outer peak.
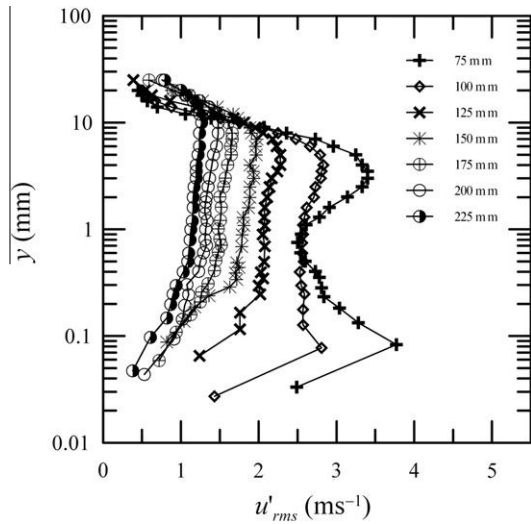
Fig. 13. LDA results for the radial velocity fluctuation profiles in physical coordinates.
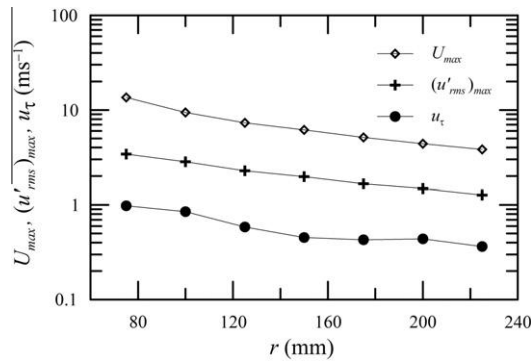

Fig. 14. Behaviour of $(u'_{rms})_{max}$ in relation to U_{max} and u_τ in physical coordinates.

The values of the outer peak in the local profiles of the rms value of u' (denoted $(u'_{rms})_{max}$) as compared to the peak values of the mean radial velocity and the friction-velocity are shown in Fig. 14 in physical coordinates. Of course, all these quantities decrease as r increases. However, and again, as expected, their decay rates are different. The peak in u'_{rms} is more persistent.

The Reynolds stresses in turbulent boundary layers have always been correlated in terms of wall variables – that is to say in terms of u_τ – so that similarity can be assessed. Typically, the development of u'_{rms}/u_τ for zero-pressure gradient flows in various Reynolds number regime shows a weak dependency on Reynolds number based on the momentum defect thickness (Fernholz and Finley [30]).

Here, to correlate the u'_{rms}, two other characteristic velocities can be used: U_{max} and U_o. The argument is that the peak in u'_{rms} is removed from the wall, so that outer flow reference velocities should be used. Fig. 15 shows the development of $(u'_{rms})_{max}$ normalized with u_τ, U_{max} and U_o. The dashed curves correspond to a straight line fit through the data of $(u'_{rms})_{max}/U_{max}$ and to a power law fit through the data of $(u'_{rms})_{max}/U_o$.

The corresponding expressions are:

$$\frac{(u'_{rms})_{max}}{U_{max}} = 0.0142\left(\frac{r}{D}\right) + 0.2696, \tag{13}$$

$$\frac{(u'_{rms})_{max}}{U_o} = 0.376\left(\frac{r}{D}\right)^{-0.969}. \tag{14}$$
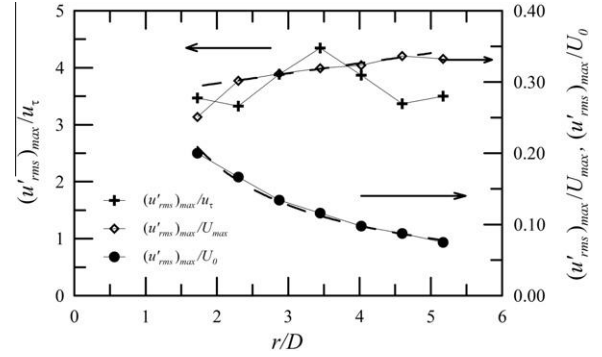

Fig. 15. The development of $(u'_{rms})_{max}$ normalized with u_τ, U_{max} and U_o.
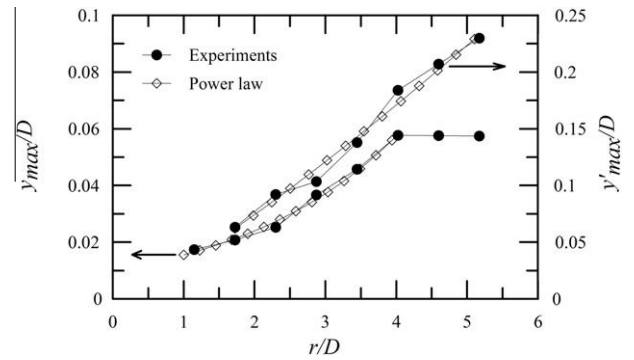

Fig. 16. The radial distribution of y'_{max}.

The linear behaviour of $(u'_{rms})_{max}/U_{max}$, with a slope that is about 1/20 of the intercept, means that over short distances changes in $(u'_{rms})_{max}/U_{max}$ will be small; to every unit of r/D, changes in $(u'_{rms})_{max}/U_{max}$ will be about 5%.

The positions at which the u'-profiles reach the outer maximum, y'_{max}, are analyzed in Fig. 16. The power law fit gives an exponent with the value of 1.203 (Eq. (15)). This value should be compared with the exponent for the growth of y_{max}, $n_2 = 0.437$.

$$\frac{y'_{max}}{D} = 0.0323\left(\frac{r}{D}\right)^{1.203}. \tag{15}$$

Of course, an analysis based on the gross parameters proposed by Narasimha et al. [27] can also be attempted to correlate $(u'_{rms})_{max}$ and y'_{max}. In this case, Eqs. (14) and (15) should be written as

$$\frac{(u'_{rms})_{max}\,v}{M_j} = D_1\left(\frac{rM_j}{v^2}\right)^{m'_1}, \tag{16}$$

$$\frac{y'_{max}M_j}{v^2} = D_2\left(\frac{rM_j}{v^2}\right)^{m'_2}. \tag{17}$$

The corresponding results are shown in Fig. 17. The power law fits furnish $D_1 = 9095.45$, $m'_1 = -0.969$, $D_2 = 0.000412$, $m'_2 = 1.203$. The worth comment here is that the exponents in Eqs. (14) and (16) are identical up to the third decimal. This is also true for the exponents in Eqs. (15) and (17).

To further characterize the spreading of the wall-jet, skewness and flatness are considered at every measuring position. In turbulent flows, important structural information can be extracted from the higher-order moments.

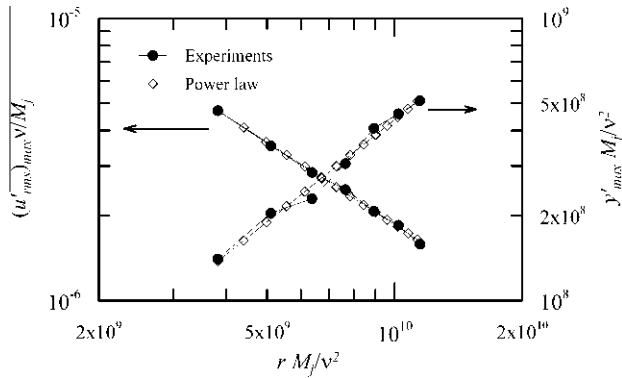The skewness and flatness factors for the radial velocity fluctuations are defined by

Fig. 17. Functional behaviour of $(u'_{rms})_{max}$ and its position, y'_{max}, in the variables proposed by Narasimha et al. [27].
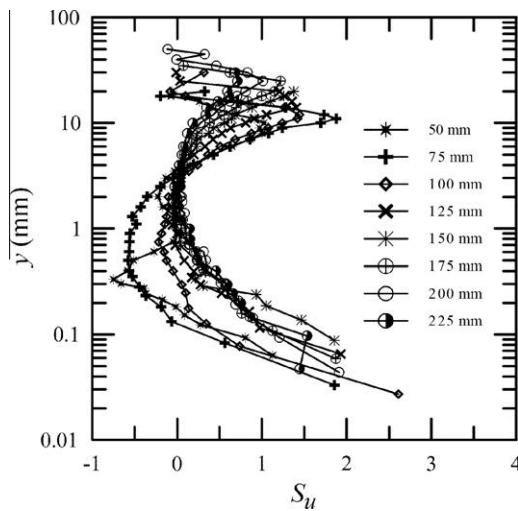

Fig. 18. Profiles of skewness.

Fig. 19. Profiles of flatness.

$$S_u = \overline{u'^3}/(\overline{u'^2})^{3/2}, \tag{18}$$

$$F_u = \overline{u'^4}/(\overline{u'^2})^2. \tag{19}$$

For an equilibrium boundary layer over a smooth wall, S_u is negative across the entire flow field (Flack et al. [31] and Krogstad and Antonia [32]). For the impinging jet, very large positive values of S_u are noted in the inner and outer regions of the flow as a result of the arrival of high acceleration-dominated velocity fluctuations originated in the unsteady shear layer of the free jet (Fig. 18). The arrival of high-speed fluid from the deflected jet means that large positive values of u'_{rms} are more frequent than large negative values. For $r < 125$ mm some intervals of negative S_u can be observed, in particular, for $r = 75$ mm. At this position, S_u is negative across the range 0.1 mm $< y < 3$ mm. The negative values of S_u result from wall-deflected upward flow. For $r \geqslant 125$ mm, there are patches where the probability distribution of u' is symmetric ($S_u = 0$). However, for most of the flow field, S_u is shown to be positive.

Profiles for the flatness in a boundary layer typically show very high values near the wall and in the outer layer – where turbulence is highly intermittent – normally not in excess to 6. For equilibrium flows, F_u is usually about 2.8 in the fully turbulent region. Fig. 19 shows the flatness distribution for the impinging jet. In the near-wall and in the outer region F_u presents sharp peaks that can attain values as high as 12 ($r = 75, 100, 125$ mm). However, for a region corresponding to 0.23 mm $< y < 5.0$ mm, F_u assumes a constant behaviour equal to 2.9, indicating that the turbulent flow is in an equilibrium state.
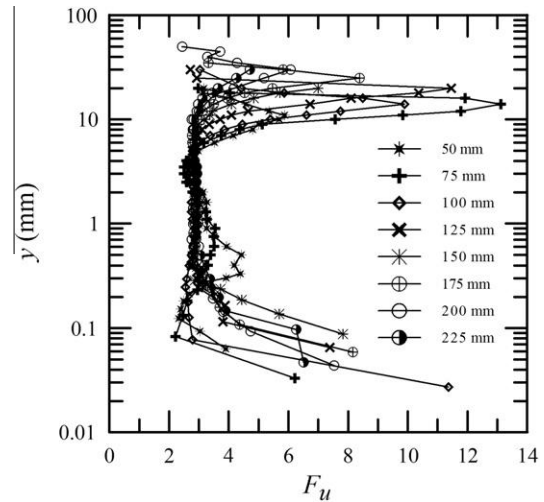
5. Conclusion

The present work has described the dynamic behaviour of a confined jet impinging over a smooth surface. Detailed near wall measurements have permitted the evaluation of the wall shear stress by means of the linear velocity profile in the viscous sublayer. Overall, the Preston tube was shown not to be capable of reproducing the behaviour of the wall shear stress.

The data were used to perform a parametric analysis of impinging jets based on propositions that resort to classical variables such as the nozzle diameter, nozzle-to-plate space and bulk velocity of the jet. Regarding the turbulent field, the classical analysis was shown to be very sensitive to the choice of the reference quantities, resulting in functional behaviours that can be represented through either power law or linear expressions. Alternatively, a second analysis of the problem was made considering some gross parameters of the jet such as its momentum flux. A discussion on the behaviour of U_{max} and u'_{rms} and their locations y_{max} and y'_{max} in terms of non-dimensional power-law expressions has also been made. It has been shown that U_{max} presents an inversely linear decay with the radial distance whereas y_{max} grows almost linearly with r. The analysis particularly shows that the jet momentum flux and the kinematic viscosity suffice to determine the mean and fluctuating flow parameters, even in the initial region of wall jet development ($1 < r/D < 5$). This indicates that the jet momentum flux M_j may actually be a very appropriate flow scaling for the parametric representation of impinging jets.

The inner layer velocity profile is shown to have a logarithmic behaviour. In particular, the level of the logarithmic profile is shown to increase with increasing maximum jet velocity. A parametrization scheme has been proposed here to describe this effect.

Finally, the dataset provided in this work – mean and turbulent quantities, impingement pressure and wall shear stress – constitutes a serious attempt by the present authors to make available benchmark results to be used in the future validation of near wall analytical and numerical models.

References

[1] Y. Guo, D.H. Wood, Measurements in the vicinity of a stagnation point, Exp. Thermal Fluid Sci. 25 (2002) 605–614.

[2] C.V. Tu, D.H. Wood, Wall pressure and shear stress measurements beneath an impinging jet, Exp. Thermal Fluid Sci. 13 (1996) 364–373.

[3] D.J. Phares, G.T. Smedley, R. Flagan, The wall shear stress produced by the normal impingement of a jet on a flat surface, J. Fluid Mech. 418 (2000) 351–375.

[4] K.G. Winter, An outline of the techniques available for the measurement of skin friction in turbulent boundary layers, Prog. Aero. Sci. 212 (1977) 615–636.

[5] J.W. Naughton, M. Sheplak, Modern developments in shear-stress measurements, Prog. Aero. Sci. 38 (2002) 515–570.

[6] N. Hutchins, K.-S. Choi, Accurate measurements of local skin-friction coefficient using hot-wire anemometry, Prog. Aero. Sci. 38 (2002) 421–446.

[7] J.B.R. Loureiro, F.T. Pinho, A.P. Silva Freire, Near wall characterization of the flow over a two-dimensional steep smooth hill, Exp. Fluids 42 (2007) 441–457.

[8] J.B.R. Loureiro, D.V. Soares, J.L.A. Fontoura Rodrigues, F.T. Pinho, A.P. Silva Freire, Water tank and numerical model studies of flow over steep smooth two-dimensional hills, Boundary-Layer Meteorol. 122 (2007) 343–365.

[9] J.B.R. Loureiro, F.B.C.C. Sousa, J.L.Z. Zotin, A.P. Silva Freire, The distribution of wall shear stress downstream of a change in roughness, Int. J. Heat Fluid Flow 31 (2010) 785–793.

[10] I.B. Özdemir, J.H. Whitelaw, Impingement of an axisymmetric jet on unheated and heated flat plates, J. Fluid Mech. 24 (1992) 503–532.

[11] D.R.S. Guerra, J. Su, A.P. Silva Freire, The near wall behaviour of an impinging jet, Int. J. Heat Mass Transfer 48 (2005) 2829–2840.

[12] C.-J. Chen, S.-Y. Jaw, Fundamentals of Turbulence Modelling, Taylor and Francis, 1998.

[13] M. Popovac, K. Hanjalic, Compound wall treatment for RANS computation of complex turbulent flows and heat transfer, Flow Turbul. Combust. 78 (2007) 177–202.

[14] T.J. Craft, A.V. Gerasimov, H. Iacovides, B.E. Launder, Progress in the generalization of wall-function treatments, Int. J. Heat Fluid Flow 23 (2002) 148–160.

[15] F. Chedevergne, Advanced wall model for aerothermodynamics, Int. J. Heat Fluid Flow 31 (2010) 916–924.

[16] R.P. Patel, Self preserving two dimensional turbulent jets and wall jets in a moving stream, M.Sc. Thesis, McGill University, Montreal, 1962.

[17] A. Tailland, J. Mathieu, Jet parietal, J. Mecanique 6 (1967) 103–131.

[18] V. Ozarapoglu, Measurements in incompressible turbulent flows, D.Sc Thesis, Laval University, Quebec, 1973.

[19] H.P.A.H. Irwin, Measurements in a self-preserving plane wall jet in a positive pressure gradient, J. Fluid Mech. 61 (1973) 33–63.

[20] G.P. Hammond, "Complete velocity profile and optimum" skin-friction formulas for the plane wall-jet, J. Fluids Eng. 104 (1982) 59–66.

[21] I. Wygnanski, Y. Katz, E. Horev, On the applicability of various scaling laws to the turbulent wall jet, J. Fluid Mech. 234 (1992) 669–690.

[22] V.C. Patel, Calibration of the Preston tube and limitations on its use in pressure gradients, J. Fluid Mech. 23 (1965) 185–208.

[23] F. Durst, H. Kikura, I. Lekakis, J. Jovanovic, Q. Ye, Wall shear stress determination from near-wall mean velocity data in turbulent pipe and channel flows, Exp. Fluids. 20 (1996) 417–428.

[24] M.J. Tummers, J. Jacobse, S.G.J. Voorbrood, Turbulent flow in the near field of a round jet, Int. J. Heat Mass Transfer 54 (2011) 4939–4948.

[25] M. Poreh, Y.G. Tsuei, J.E. Cermak, Investigation of a turbulent radial wall jet, Trans. ASME J. Appl. Mech. 34 (1967) 457–463.

[26] S. Beltaos, N. Rajaratnam, Circular turbulent impinging jet, J. Hyd. Div. ASCE 100 (1974) 1313–1328.

[27] R. Narasimha, K.Y. Narayan, S.P. Pathasarathy, Parametric analysis of turbulent wall jets in still air, Aeronaut. J. 77 (1973) 335–339.

[28] J.B.R. Loureiro, A.S. Monteiro, F.T. Pinho, A.P. Silva Freire, Water tank studies of separating flow over rough hills, Boundary-Layer Meteorol. 129 (2008) 289–308.

[29] K. Kataoka, Y. Kamiyama, S. Hashimoto, K. Komai, Mass transfer between a plane surface and an impinging jet, J. Fluid Mech. 119 (1982) 91–105.

[30] H.H. Fernholz, P.J. Finley, The incompressible zero-pressure-gradient turbulent boundary layer: an assessment of the data, Prog. Aero. Sci. 32 (1996) 245–311.

[31] K.A. Flack, M.P. Shultz, J.S. Connely, Examination of a critical roughness height for outer layer similarity, Phys. Fluids 19 (2007) 95–104.

[32] P.A. Krogstad, R.A. Antonia, Surface roughness effects in turbulent boundary layers, Exp. Fluids 27 (1999) 450–460.